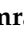




Article

A Novel Light U-Net Model for Left Ventricle Segmentation Using MRI

Mehreen Irshad ¹, Mussarat Yasmin ¹, Muhammad Imran Sharif ¹ , Muhammad Rashid ² ,
Muhammad Irfan Sharif ³ and Seifedine Kadry ^{4,5,6,7,*} 

¹ Department of Computer Science, COMSATS University Islamabad, Wah Campus, Wah Cantt 47010, Pakistan

² Department of Computer Science, University of Turin, 10124 Turin, Italy

³ Department of Information Sciences, University of Education Lahore, Jauharabad Campus, Jauharabad 41200, Pakistan

⁴ Department of Applied Data Science, Noroff University College, 4612 Kristiansand, Norway

⁵ Artificial Intelligence Research Center (AIRC), Ajman University, Ajman P.O. Box 346, United Arab Emirates

⁶ Department of Electrical and Computer Engineering, Lebanese American University, Byblos 13-5053, Lebanon

⁷ MEU Research Unit, Middle East University, Amman 11831, Jordan

* Correspondence: seifedine.kadry@noroff.no

Abstract: MRI segmentation and analysis are significant tasks in clinical cardiac computations. A cardiovascular MR scan with left ventricular segmentation seems necessary to diagnose and further treat the disease. The proposed method for left ventricle segmentation works as a combination of the intelligent histogram-based image enhancement technique with a Light U-Net model. This technique serves as the basis for choosing the low-contrast image subjected to the stretching technique and produces sharp object contours with good contrast settings for the segmentation process. After enhancement, the images are subjected to the encoder–decoder configuration of U-Net using a novel lightweight processing model. Encoder sampling is supported by a block of three parallel convolutional layers with supporting functions that improve the semantics for segmentation at various levels of resolutions and features. The proposed method finally increased segmentation efficiency, extracting the most relevant image resources from depth-to-depth convolutions, filtering them through each network block, and producing more precise resource maps. The dataset of MICCAI 2009 served as an assessment tool of the proposed methodology and provides a dice coefficient value of 97.7%, accuracy of 92%, and precision of 98.17%.

Keywords: left ventricular segmentation; MRI; deep learning; image enhancement technique; histogram

MSC: 68U10



Citation: Irshad, M.; Yasmin, M.; Sharif, M.I.; Rashid, M.; Sharif, M.I.; Kadry, S. A Novel Light U-Net Model for Left Ventricle Segmentation Using MRI. *Mathematics* **2023**, *11*, 3245. <https://doi.org/10.3390/math11143245>

Academic Editor: Radu Tudor Ionescu

Received: 23 May 2023
Revised: 17 July 2023
Accepted: 18 July 2023
Published: 24 July 2023



Copyright: © 2023 by the authors. Licensee MDPI, Basel, Switzerland. This article is an open access article distributed under the terms and conditions of the Creative Commons Attribution (CC BY) license (<https://creativecommons.org/licenses/by/4.0/>).

1. Introduction

The world is facing a huge amount of human death mainly caused by cardiovascular diseases (CVD), i.e., 17.3 million deaths every year, which may reach the limits of more than 23.6 million by 2030 [1]. It dramatically impacts both developed and non-developed countries, no matter the countries with higher income. CVD comprises heart failure, ischemic heart diseases, peripheral arterial disease, stroke, and many other vascular conditions, which are key contributors to life reduction [2,3]. Around 9.6 and 8.9 million males and females passed away due to CVD in 2019, i.e., an estimated one-third of the total deaths worldwide.

For diagnosing cardiac diseases, it is necessary to quantify Left Ventricle (LV) function. Since precise LV contours [4] provide much information regarding its size and shape, segmenting LV is critical in estimating the key diagnostic indicators [5]. Numerous segmentation methods are used to increase the robustness and correctness of results. LV

segmentation from cardiac magnetic resonance images provides significant supplementary data for the analysis and treatment follow-up of CVD ailments, the fundamental cause of death worldwide [6].

Customarily, the LV segmentation expedition is accomplished physically, which is monotonous, tedious and needs lots of human involvement and expertise to produce segmentation results [7]. Moreover, occasionally the specialists/clinicians neglect to contract an enormous arrangement of information. So, the specialists presented a semiautomatic framework for the procedure's part to surface the outcomes. These systems are undoubtedly taking many times and need experts with full concentration. Furthermore, accuracy in results and fastness require the automaticity of systems. One step towards this is semi-automatic systems, but nowadays, technological advancement opens the door to moving to the fully automatic system.

The automatic algorithms can deal with tedious searches and manage enormous information measures to investigate the local and worldwide capacity of heart MRI-LV by computing clinical parameters like EF (Ejection Fraction), ESV (End Systolic Volume), EDV (End Diastolic Volume) and myocardial mass [8].

The difficulties in automatically segmenting the Left Ventricle incorporate managing the existence of papillary muscles in feeble edges around the epicardium of the Left Ventricle, which will be managed properly without the consideration of manual adjustment of conclusive outcomes. At long last, the changeability in the state of the endocardium and epicardial forms crosswise over cuts and stages, which make the myocardium exposure much more complex, will likewise be considered in the proposed work. To put it plainly, the proposed framework will lessen the measure of time required for the examination of heart work and segmentation. A few major steps for the proposed method include data preparation, preprocessing, and the light U-Net model. The major contributions made in this proposed method correspond to the following steps.

Contributions

- An image normalization method is performed prior to processing. The efficiencies of the proposed algorithm are strongly impacted by the enhancement of image contrast. Improving an image's contrast is surely a prerequisite for image processing.
- Intelligent Contrast Stretching and Histogram Equalization improves an image that has already undergone preprocessing with unsharp masking.
- The Encoder path implanted layers with convolutional blocks and reducing the batch layer while in next layer removing the activation layer as well.
- Afterward, up-sampling enlarges the feature batch back to its actual size. The significant contribution of the proposed technique is to provide 99% precise results of the epicardium layer.
- The test dataset includes LVOT (Left Ventricle Outflow Tract) images of both endocardium and epicardium.

An analytic overview of previous research is depicted in further segments. Then, the novel contribution is introduced as an intelligent image enhancement technique that will not apply to all images from the dataset but only to the low-contrast images, which require preprocessing. Afterward, a novel deep learning model which utilizes the stock U-Net model as the backbone and is optimized to a lightweight model is mentioned along with its results and analytical discussion.

2. Related Work

Diseases related to the heart are the leading cause of death nowadays. Certain advancements are being made continuously to detect cardiac illness on time. Automatically limiting the cardiovascular MR images to specific areas of LV is an essential step to automated procurement post imaging and planning analysis, for example, function and segmentation examining errands. Cardiovascular MRI adds a useful asset for analyzing the capacity and imaging the heart structure [9]. The diseases are either detected by manual or automated

segmentation analysis. Manual delineation is slow and tedious because of the huge amount of data acquisition. So, automated segmentation is the demand which is quick, precise, and helps to encourage cardiac problems analysis [10].

Basic image-based methodologies [11,12] involving threshold, shape models, active contours, region-based techniques, level sets, and graph-based techniques are used to develop automatic segmentation systems and succeeded in attaining over 90 percent of segmentation results. Image segmentation using thresholding is easier; however, the approach is powerful for segmenting images having lighter objects on darker backgrounds [13,14]. Segmentation of images in medical is yet a main issue due to the lack of contrast among tissues and the contextual, substantial noises and boundaries of indistinct objects. In recent eras, methods of profile-based image segmentation with ASM (active shape model) [15,16] and AAM (active appearance model) [17,18] have drawn much devotion. ASM has exposed its potential in object detection and extraction of features.

Atlas-based methodologies are used to convert the segmentation problem into a registering problem [19,20]. Among the most recent research [21], ACM is applied to MICCAI 2009 cardiac dataset, another Global Local Region-Based ACM, in combination with watershed [22]. Similarly, a combination of extended random walk and high-speed random walk [23] and the ACM-based technique, along with region-based segmentation [24], obtained a good dice value of 0.986. The level sets-based technique [25] showed good results for segmentation. Another two-layered level set using a circular shape constraint [26] shows DM (Dice Metric) (Endo: 0.92, Epi: 0.94) and APD (Endo: 1.77, Epi:1.85). The multi-atlas-based segmentation [27] technique is used for myocardium segmentation. Many efforts have been adapted in the vast field of cardiology, including AI (Artificial Intelligence), ML (Machine Learning), CV (Computer Vision) and DL (Deep Learning) constitute a set of tools to increase the effectiveness of the cardiologist [28]. The most commonly used AI methodologies are neural networks [29]. These DL methods are being used for automatic image segmentation of the heart for evaluation of cardiac functions and mass parameters via various numbers of datasets [30,31] and providing effectiveness in results.

DL has recently demonstrated better performance and enormous potential in a number of sectors. CNN (Convolutional Neural Network) is among the extensively used DL techniques [32–37]. As a result of the quick growth of AI, particularly DL, image segmentation techniques have accomplished appropriate results [38]. DL provides several benefits over conventional ML and CV techniques in relation to segmentation accuracy and speed [39]. The application of DL to segment medical photos can, therefore, efficiently assist clinicians in confirming the size of sick tumors, quantitatively evaluating the effect before and after therapy, and significantly decreasing their burden. When it comes to image classification, DL plays a vital role. Due to the dominance regarding accuracy when trained with large amounts of data, DL has achieved much popularity. DL has two phases; encoding and decoding. The encoding phase was utilized for cardiac MR image portrayal and classification of the pixel-level data, and the phase of decoding was utilized to reestablish the first image's resolution. The red color indicates the region of LV more readily shows the segmentation [40].

Recently, DL has shown extraordinary potential and good performance in different fields. Among DL techniques, CNN is the most broadly utilized [32,37,41–50]. Until now, CNN structures are best considered for entire image cataloguing. Still, CNNs can likewise be utilized for the segmentation of images. CNN-based segmentation algorithms have abilities to solve numerous issues, particularly in the analysis of medical images, as they have shown their extraordinary accuracy [51] and robustness in the past recent years [52,53]. With the advancements in CNN [54–60], the majority of the fields in pattern identification and CV experience a tremendous improvement and revolution, including image cataloging, object recognition and image segmentation.

It is mostly DL techniques that use CNN [61], in addition to variants and hybrid techniques such as Dense R-CNN, dual-attention, up-sampling, dilated convolution, bilinear interpolation [62], Multi-channel DL [63], CNN, and multi-scale features with a dynamic

pixel-wise weight model for LV segmentation [55]. Moreover, FCNNs (Fully Convolutional Neural Networks) [64] show good dice (Epi: 0.94 ± 0.02 , Endo: 0.96 ± 0.02) results. There has also been a YOLO-based network generated for LV segmentation [65]. ACNN (Anatomically Constrained CNN) [37] and FCNN [45] also produce good segmentation outputs.

3. Data and Method

The processing flow of the deep learning-based novel technique is shown in Figure 1. The major starting procedure includes the preparation of data, i.e., resizing of input images and pixel-wise normalization of resized images.

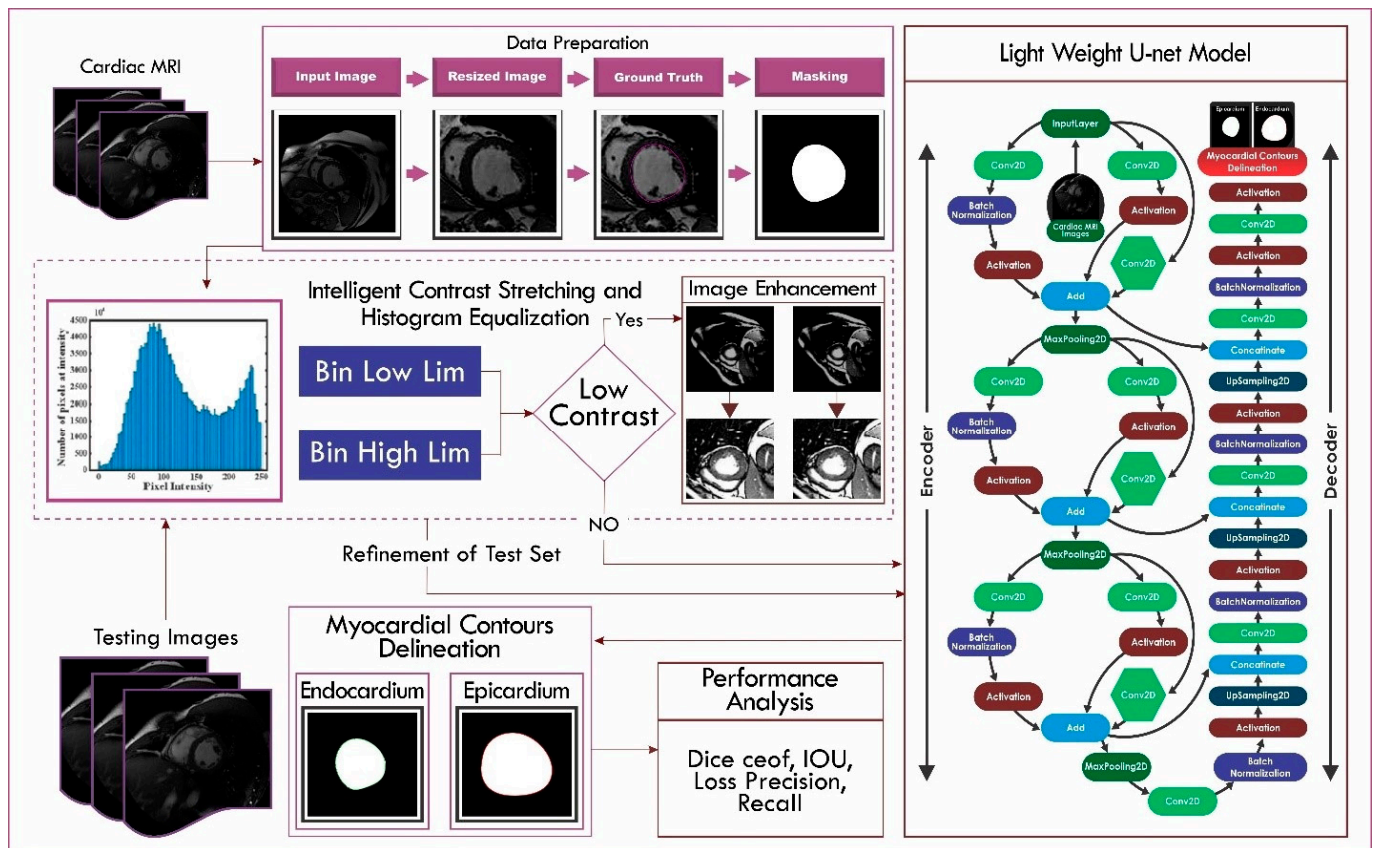


Figure 1. Phases of the Light U-Net model.

Then contrast adjustment of these images is done using Novel Intelligent Histogram Based Decision (IHBD). The next step is to train the network with the novel Light U-Net model-optimized algorithm using 2-D convolution in a distinctive hierarchal fashion. Normalization and activation are also performed in layers. The training model works to produce delineations of endocardium and epicardium. In the end, testing of the trained model is performed for extracting the segmentation of LV contours from the images of the dataset.

For evaluation purposes, the dataset of the MACCAI 2009 challenge was used. It is composed of dicom short axis, 1.5 T MR images of 45 different patient cases. Patients included are heart failure, ischemic heart failure, non-ischemic heart failure, and some normal patients are also included. The dataset provides ground truths as well. The total number of images in the dataset is 7365, including all diastolic and systolic images ranging between the complete slices of the heart.

3.1. Preprocessing: Intelligent Contrast Stretching and Histogram Equalization

The absolute requirement of image processing is the contrasting enhancement of an image. Improving visual parameters and reducing illumination issues of LV in a gray

image is significant for achieving promising results. Since the data was in its raw form and presented very blurry images, the first step was to normalize the image's pixels. The images mostly had good contrast, but in the case of a few images, the contrast was either very high or very low, which could cause less segmentation accuracy.

To deal with this issue, the IHBD (Intelligent Histogram-Based Decision) method is proposed, which can decide whether the image has low contrast. Once dataset images are classified into a low-contrast image set, these images are passed to the image enhancement module. [66]. Figure 2a shows the images with ground truth drawn from the dataset having different contrasts. Figure 2b represents the histogram of these images. A horizontal axis is assigned for the color scale representation, while the vertical values on the axis depict the frequency of image pixels for that specified shade. Most of the information is occupied by unilluminated areas of the generated histogram. The very first step is to generate a histogram for all input images. Then, from the histogram, a limit value as a bin low and a peak limit value is calculated for the input image. Furthermore, a function is performed to classify the images into low-contrast ROI and normal ROI by performing a comparison with each other, depending upon the image's bin values. This is the point of decision-making using the bin values from the histogram of input images. If the value of the low bin limit is higher than the heuristic value (a value of 10 or a higher limit less than the speculative constant 240), then the image is treated as a normal image, and if not, the image is treated as a low-contrast image.

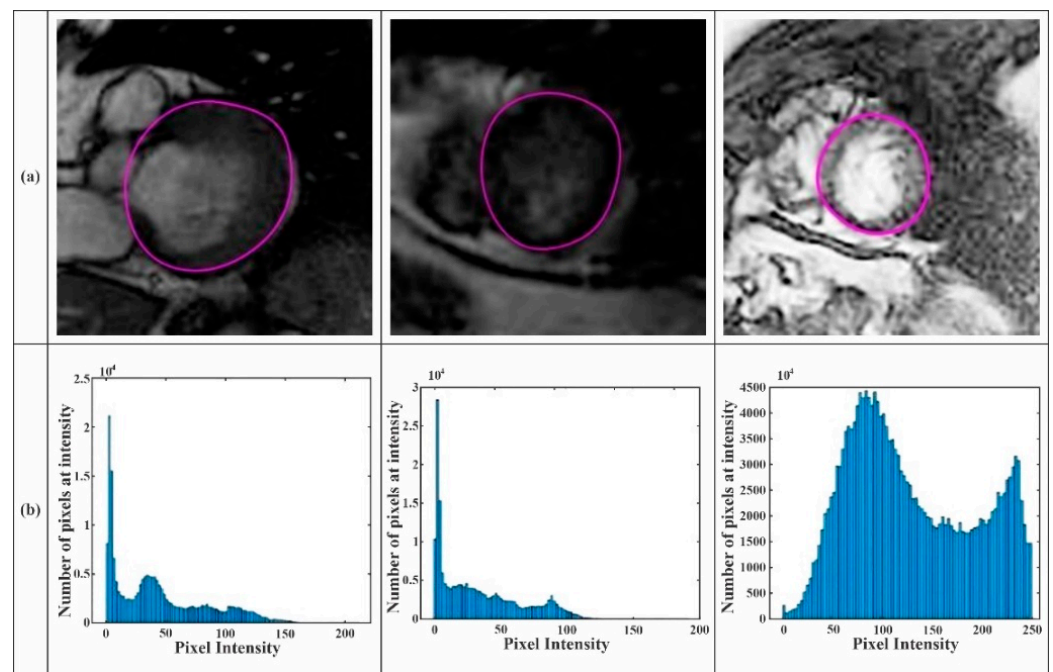


Figure 2. LV images with histogram: (a) low-contrast input image and (b) histogram for the image.

Then, after this decision is made, the problem of less distinctive shades in the images is handled through a contrast stretching approach. Similarly, the ROIs with normal contrast are forwarded to the novel segmentation process without passing it to the contrast stretching step. Ultimately, the “bin high and low limit” can be selected from the histogram features as the most relevant to this decision-making. The function of contrast stretching is accomplished through MATLAB by the stretch lim function. The histogram details the comparison of low-contrast and high-contrast images, as shown in Figure 2b.

Table 1 shows that normal sample images from the dataset have a smaller number of bins, and the low-contrast images have a large number of bins. Low-contrast images have less separation of values from the low limit to the high limit, while normal images have

more value separation. Hence, the sequence of steps for the decision-making using IHDB is clearly mentioned in Algorithm 1.

Algorithm 1. Algorithm for IHBD.

Input: Image (I)

Output: Segmented endocardium and epicardium contours

Begin

```

    Calculate bin low and bin high limit:  $\forall\{I\}$  (all images of the dataset, including LVOT, to apex)
    while (I  $\neq$   $E_{maxi}$ )
        If the low limit of the image is greater than the heuristic constant of 10
            Or
            the high limit of the image is less than the heuristic constant of 240
        Then image(I) belongs to low-contrast images
            Pass the image for contrast stretching process
        else Image is a normal image
        end If
    end while

```

end

Table 1. Histogram Values for Low-Contrast and Normal Images.

Type of Image	Feature	Sample 1	Sample 2	Sample 3
Low-Contrast Image	Bin Counts	95	166	148
	Bin Edges	96	167	149
	Bin Limits	20	34	46
	High Limit	210	200	194
	Bin Width	2	1	1
Normal Image	Bin Counts	51	64	51
	Bin Edges	52	65	52
	Bin Limits	0	63	0
	High Limit	255	255	255
	Bin Width	5	3	5

The process of IHBD is performed on the whole dataset as E_{maxi} represents a maximum number of images i from the dataset and hence all images are separated into low-contrast and normal images.

Table 2 shows that in the case of endocardial contour, 2495 images are low-contrast, and 4870 images are normal images, which clearly shows that 33.87% of the data has low-contrast images in the case of endocardial contour. In the case of epicardial contour images, 2247 are low-contrast images, and 5118 images are normal images, which shows that 30.5% of images are low-contrast images. Hence the low-contrast images need to be normalized.

Table 2. Distribution of Images into Low-Contrast and Normal Images.

Sr. No.	Type	Images		
		Total	Low Contrast	Normal
1	Epicardium	7365	2495	4870
2	Endocardium	7365	2247	5118

The histogram equalization uses pixels edge points data. A variational platform is generated depending upon existing differences in the intensity of ROI pixels and shade variations of its neighbor pixels. The following Equation (1) is used for generating the variational map P_i .

$$P_i(e, f) = \begin{cases} S_I(x, y), & \text{if } S(x, y) = g \text{ and} \\ & (|S(x, y) - S(x, y - 2)| > thresh) \\ 0, & \text{elsewhere} \end{cases} \tag{1}$$

where P_i is a variational platform, S_I represents the input image sample at x and y position, S represents the set of all images g represents the distinct intensity range for the low-contrast image, and it ranges between '0' to $Q - 1$. Q represents the frequency of different intensities. After deep analysis, $thresh$ is selected to have a value of '15' for this case. Histogram is figured using a variational platform as in Equation (2).

$$HE(P_i) = \sum_{j=1}^M \sum_{k=1}^N (P_i(j, k)) \text{ for } 0 \leq i \leq Q - 1 \tag{2}$$

where $HE(P_i)$ depicts the histogram of the variational platform. M represents rows, and N represents columns of pixels in S_I input image. Next, a probability density function (pdf) for $R(i)$ from the histogram, which can be quantified using Equation (3), which normalizes the count values.

$$R(i) = \frac{HE(P_i)}{\sum_{q=0}^{L-1} HE(P_q)}, \text{ for } 0 \leq i \leq Q - 1 \tag{3}$$

Variational platform P_i is iterated with q , and $T(i)$ denoting cumulative distribution function (CDF) is computed using Equation (4) using a discrete function $R(i)$.

$$T(i) = \sum_{j=0}^k R(i), \text{ } 0 \leq k \leq Q - 1 \tag{4}$$

where pdf is iterated with samples ranging to k from the $R(i)$ as in Equation (3). Here $W(i)$ is a mapping function that is calculated through CDF, as given in Equation (5).

$$W(i) = (Q - 1) \times T(i) \tag{5}$$

The $W(i)$ is iterated with the probability distribution function and multiplied by the cumulative distribution function. Finally, the structure of the enhanced image is preserved using a guided filtering process.

The proposed intelligent contrast stretching is demonstrated in Figure 3. Low-contrast images are shown in row Figure 3a; all images are clearly dark, having pixels values closer to 0. These images are processed through the image adjust function, which maps the pixel values to equalize in weights within the acceptable limit of contrast, as shown in Figure 3b. The final mapping of adjusted pixels on the image is shown in Figure 3c. Results show prominent enhancement in contrast to images. A mathematical evaluation of these images or the performance of this enhancement algorithm is tested through PSNR values calculations as shown in Figure 3d. PSNR values are prominently showing remarkable achievement as given images in Figure 3 have values as 54.95, 54.43, 54.2698 and 54.6299.

Image Names	IM-0001-0441	IM-0001-0797	IM-0001-7146	IM-0001-5557
Low Contrast Input Image (a)				
Adjusted Image (b)				
Proposed Enhanced Image (c)				
PSNR Values (d)	54.9518	54.4377	54.2698	54.6299

Figure 3. Image preprocessing: (a) low contrast input image, (b) adjusted image, (c) proposed enhanced image, (d) PSNR values.

3.2. Light Deep Learning U-Net Model

A generalized perspective of the proposed Light U-Net network is that the encoder uses weights from the database [67]. The pre-trained encoder, built on structures, combines spatial convolutions with 3×3 kernel size, ReLU activation, and layers of batch normalization and inserts 256×256 pixel input images into the proposed model. In this instance, the encoder will filter and learn the properties of the images, feeding the network using compact depth-to-depth convolution. By reducing the number of parameters, these inverted blocks make it simpler and quicker to train the model.

A pre-trained network has the added benefit of improving the model’s performance and accelerating convergence. The up-sampling procedures are performed in the decoding route to expand the feature map back to its original size. This approach involves concatenating the characteristics between the encoder and decoder blocks, as well as passing them via a 3×3 convolution layer, batch normalization, and sigmoid activation. In order to construct the segmented map, the last block in the network contains a 1×1 convolutional layer and a sigmoid activation. The stepwise description of the proposed model is depicted in Figure 4. This U-Net is built on the basis of the architecture of CNN with suitable adaptations to the nature of grayscale MR images. The root elements used as a building block of the proposed Light U-Net model are also mentioned in Figure 4.

The encoder and decoder paths are preliminary to the U-Net architecture. Here, for Light U-Net, both are utilized to achieve the desired training. The layers utilized are the convolutional layer, max pooling, ReLU activation, sigmoid activation functions, concatenation, and recollecting as up-sampling is applied to reach the endpoints of the deep net model. The data propagate through these network paths of encoding, decoding and successions.

For training, the original ROI is provided as input to the U-Net model. The encoder block (Eb) and decoder block (Db) make up the U-Net. The encoder and decoder blocks are constituted by two 3×3 convolutional layers that are repeated (double-conv). The design of the encoder block contributes uniqueness as three convolutional layers are used

in parallel and each with one less additional layer of batch normalization and activation stepwise. When comparing Eb with Db, Db links a reverse convolution layer after double-convolution, and Eb connects a max-pooling layer after double convolution. After applying double convolution, a dense block transfers and adds a 1x1 convolutional layer to provide the final segmentation output.

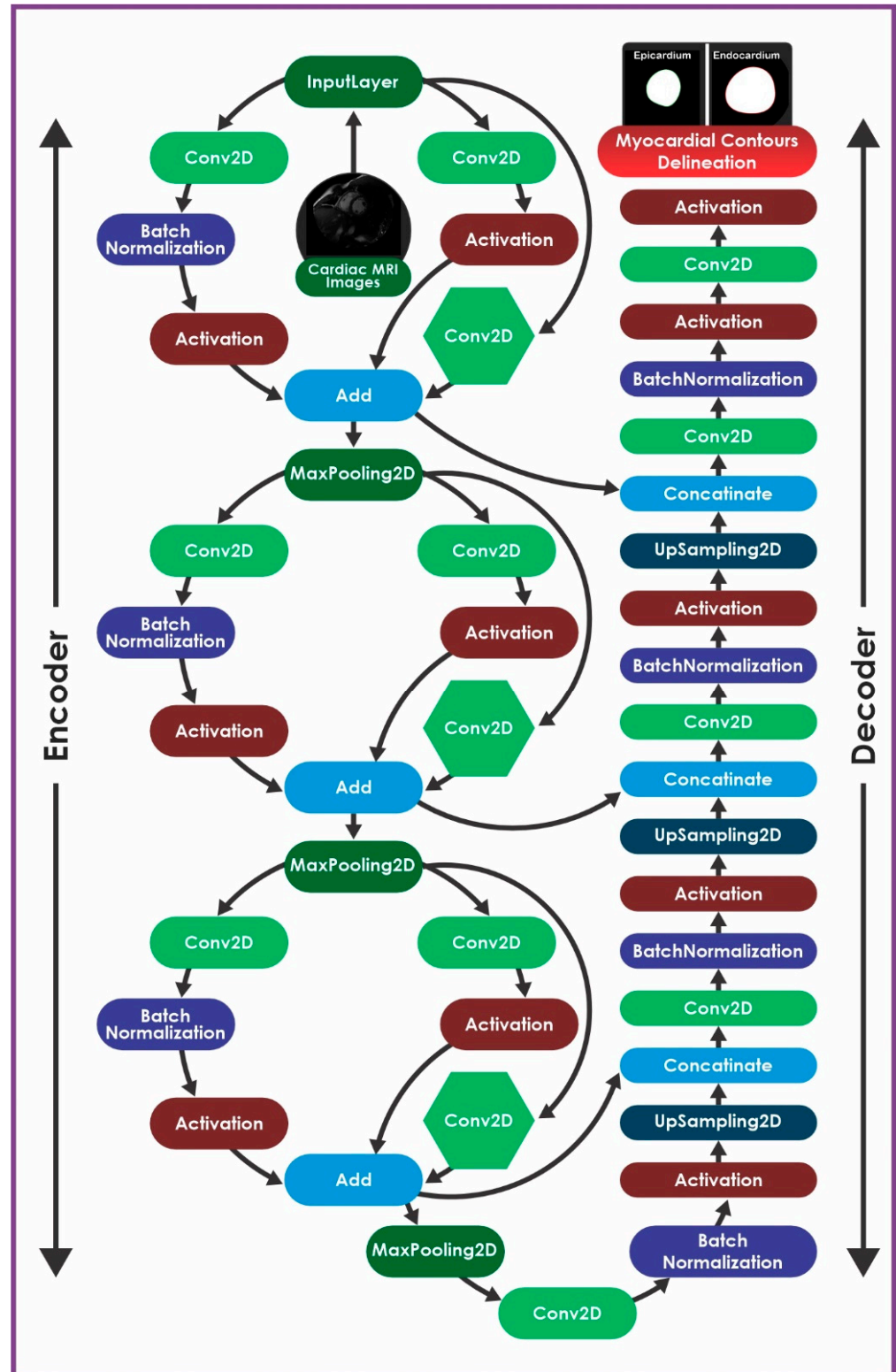


Figure 4. Novel light U-Net model for LV segmentation.

The design of the model is depicted layerwise in Figure 4; a multiplexed convolutional operation starts from the input, and the first convolutional block is a complete set of batch normalization and activation functions. In parallel, the second convolutional block, as a comparison to the first, skips batch normalization; similarly, following this reducing pattern, the third block consists of only one convolutional layer. All these collectively add up to the next layer and concatenate to the decoder block as well. The design of the decoder side is in a smooth fashion, one above the other convolutional blocks with batch normalization, activation and up-sampling. The design of the model is shown in Figure 4.

Finally, the softmax function and a 1×1 convolution layer are utilized for convexing the extended feature set to 2 so it can produce the predicted segmentation, as mentioned in Equation (6).

$$g_{i,j}^x = \frac{\exp(s_{i,j}^x)}{\sum_{x'=1}^2 \exp(s_{i,j}^{x'})} \tag{6}$$

where $s_{i,j}^x$ stands for the generated value of x th number channel at coordinates i and j of the output map, $g_{i,j}^l$ stands for the SoftMax value of x th number of channels at i and j coordinates of the output map, and $x = 1, 2$. The cross-entropy function yields the following cost function (Equation (7)).

$$a_u = \sum_{i=1}^{128} \sum_{j=1}^{128} - \sum_{x=1}^2 h_{i,j}^x \log(g_{i,j}^x) \tag{7}$$

where the ground truth channel is at the x th level is indicated by $h_{i,j}^x$ at the given locations. Then, the cost function is reduced using the gradient descent algorithm as given in Equation (8).

$$\check{T}, \check{c} = \arg \min_{T,c} a_u \tag{8}$$

where \check{T}, \check{c} are the symbols used for all U-Net parameters. A model was obtained that was almost optimum after training. To obtain a dual-channel output of $g \in R^{2 \times 128 \times 128}$, the unprocessed-ROI is inserted as raw input into the training zone of U-Net. The following formula yields the final binary mask g as in Equation (9).

$$g_{i,j} = \begin{cases} 0, & g_{i,j}^1 \geq g_{i,j}^2 \\ 1, & g_{i,j}^1 \leq g_{i,j}^2 \end{cases} \tag{9}$$

4. Results

The framework is implemented using the Spyder (Python 3.9) NN deep learning framework as the training phase. Adam optimizer is also used as an optimizer. The time taken by the system to perform each step is 2 s. In this approach, the starting learning rate at a value of 0.001 was decomposed by 0.95 at each epoch, and the weight deterioration (L2 regularization) was adjusted at 1×10^{-4} . The experiments are executed on an NVIDIA RTX 3070 GPU.

The TensorFlow [68] framework was used as a backend, and the Keras [69] library as a frontend to construct the suggested model. The training and testing subsets of the MICCAI 2009 data set are each given a proportion of 70% and 30%, respectively. The training is conducted using a 0.0001 learning rate, handling with a batch width of 16, the selected optimizer being Adam, and the model is trained up to 100 epochs before convergent executing 76 epochs. In order to further prevent overfitting, early stopping regularization is applied to the validation subset, especially to the validation loss. It took 4 h to finish the network’s training.

Formulated gauges help to measure the performance of newly explored techniques. Among these standard measures, the most used are the dice metric (DM), accuracy, average perpendicular distance (APD), the intersection of union (IoU), recall and precision. The

dice metric reports the execution of unwavering quality in terms of manual segmentation consequences and pixel-wise overlapping of the generated map. In the equation intersection, \mathfrak{B} represents the segmented points by novel approach, \mathfrak{C} is the sign used for manual results of segmented points. Hausdroff distance (HD) is a measure that shows the distance between the ground truth contour and the segmented region. Intersection-over-union (IoU) is determined sequentially through the images between ground truth (GT) and predicted segmentation (IP). The recall measures the similarity proportion between the algorithm-calculated boundary and the boundary of ground truths. As in the equation below, the \mathbb{RCL} represents recall. \mathbb{PR} and \mathbb{G} represent the results of the proposed technique and gold standard manual contours. The precision is another scale that measures the sameness of ground truths and the proposed result. In other words, we can say it is a probability of valid results. The equation below shows $\mathbb{P}\mathfrak{C}$ as precision. \mathbb{PR} and \mathbb{G} represent the results of the proposed technique and ground truth contours. These equations are given below.

$$\text{Dice matrix } d^m = i / [\check{c} \times (\mathfrak{B} + \mathfrak{C})] \tag{10}$$

$$\text{Hausdroff distance } HD = \max(\max_{j \in [0, O - 1]} d(j, GT, P), \max_{j \in [0, M - 1]} d(j, P, GT)) \tag{11}$$

$$\text{Jaccard index } \text{IoU}(GT, IP) = \frac{|GT \cap IP|}{|GT \cup IP|} \tag{12}$$

$$\text{Accuracy} = \frac{TP + TN}{TP + TN + FP + FN} \tag{13}$$

$$\text{Precision } \mathbb{P}\mathfrak{C} = \frac{\text{Match}(\mathbb{PR}, \mathbb{G})}{|\mathbb{PR}|} \tag{14}$$

$$\text{Recall } \mathbb{RCL} = \frac{\text{Match}(\mathbb{PR}, \mathbb{G})}{|\mathbb{G}|} \tag{15}$$

4.1. Experiment 01: LV Endocardium Segmentation Results

A hyperparameter that manages the quantity at the base of gradient descent for iterations over the full training dataset is its quantity of epochs. When the subsequent cycle of the same dataset simulation occurs, known as the next epoch, the weights that were initially established will be subject to changes. Underfitting and Overfitting are the two fundamental issues that plague epoch optimization. An optimization of gradient descent iteratively adjusts the weights of the neural network. The network underfits the data if we train it for only a few epochs. This indicates that the neural network is unable to detect the data’s underlying trend. An increase in epochs eventually reaches an ideal state where we will obtain the greatest accuracy on the training set, which consequently provides improved results on the testing set. If we continue to increase the number of epochs after this point, the data will become overfit. A hypermeter requires tuning, and we cannot predict in advance how many epochs would be needed to achieve the optimum level of training. To train the neural network, we can only employ a few heuristics and a fixed number of epochs while keeping an eye on the precision of the testing results.

In Table 3, when 20 epochs were used, the initial values in terms of accuracy, dice coefficient, IoU, loss and precision were low. With the upsurge in the number of epochs, the values are increased continuously, gained precision and yielded good results. Increasing the number of epochs, in the beginning, showed much difference in the values optimistically. However, as the number of epochs reached nearly 60, the learning rate now showed less increase and attained the maximum accuracy from a certain number of epochs. The endocardium showed a 92.7% accuracy and precision ranging to 98.17%, i.e., a good result. The dice coefficient reached up to 97.1%.

The novel technique of deep learning shows promising results for all slices of the heart and for all phases of the heartbeat, i.e., both systolic and diastolic. In addition, this novel approach shows good results for the LVOT images as well, which are extremely difficult images to segment. Randomly, a few images from different cases are selected to show the visual results of the proposed novel deep learning model, which are shown in Figure 5.

Table 3. Results of endocardium segmentation using dataset through proposed model based on epochs.

Epochs	Accuracy%	Dice Coefficient%	IoU%	Loss%	Precision%
20	0.911231	0.9444	0.9506	0.0163	0.9662
25	0.9115	0.9568	0.9551	0.0146	0.9681
30	0.9116	0.9577	0.9567	0.0139	0.9701
35	0.9116	0.9598	0.9569	0.0138	0.9707
38	0.9116	0.9608	0.9570	0.0138	0.9715
40	0.9117	0.9645	0.9571	0.0137	0.9751
42	0.9117	0.9662	0.9571	0.0137	0.9772
51	0.9119	0.9682	0.9598	0.0132	0.9798
60	0.9270	0.9712	0.9673	0.0120	0.9817

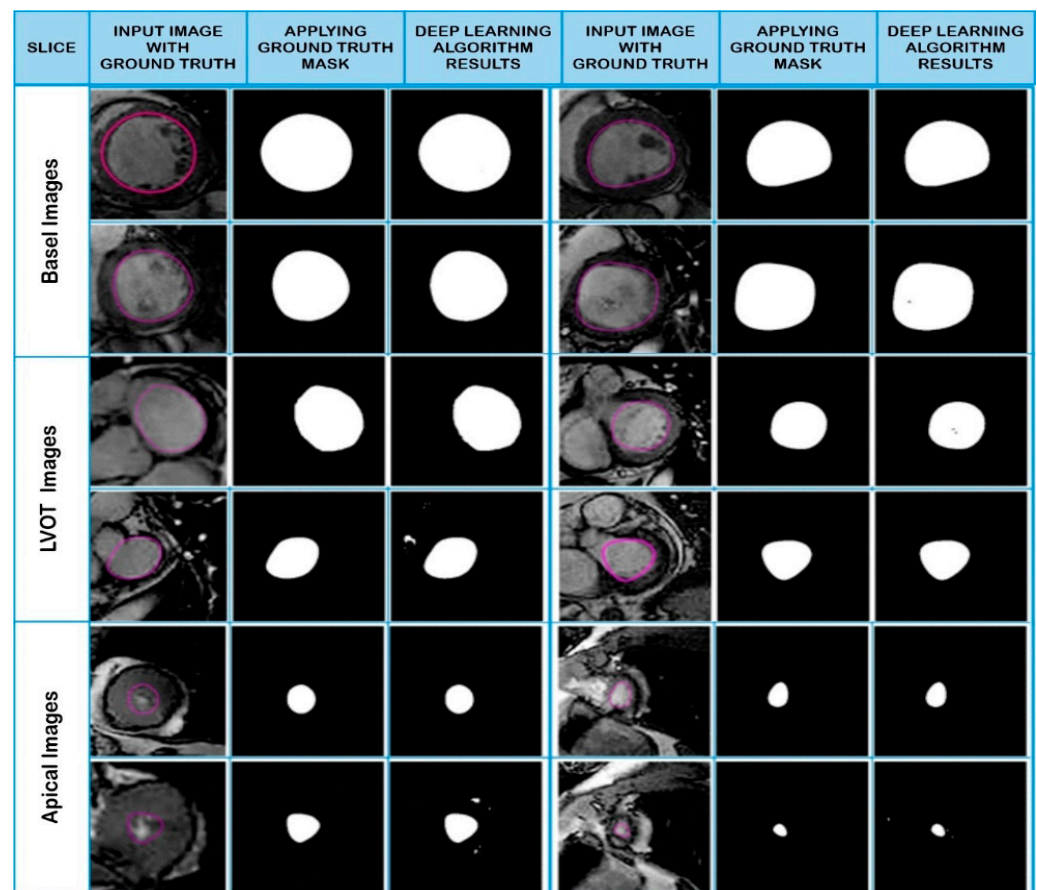


Figure 5. Segmentation results of endocardium using novel Light U-Net segmentation model.

Figure 5 is divided into three columns. The first column shows the input image of LV with the ground truth. The second column shows the mask being applied on the ground truth images. Lastly, after the mask is applied, we get the results of the novel deep learning algorithm Light U-Net applied on the ground truth images. The results are clearly showing the remarkable performance of a novel deep-learning algorithm. Images from the basal

slice, apical slice and LVOT are shown in the figure. The purpose of this comparison is to show the difference and improvement achieved after the implementation of the novel Light U-Net model against the U-Net model on endocardial images of the dataset. Figure 6 shows the performance range through graphical representation in terms of accuracy, dice measure, IoU, loss, precision, and recall values of the endocardium against a number of epochs. The blue and red lines in Figure 6 show the training and testing results of the novel Light U-Net model, respectively, while the U-Net model’s training and testing are indicated using green and purple lines, respectively. Here, in Figure 6a, the accuracy of the proposed model can be clearly seen to improve and is more targeted than the U-Net model. Figure 6b shows the dice coefficient curves. In the initial epochs, the dice coefficient has increased spontaneously, but after crossing 15 epochs, the learning rate has slowed down, and the maximum results are achieved at 60 epochs.

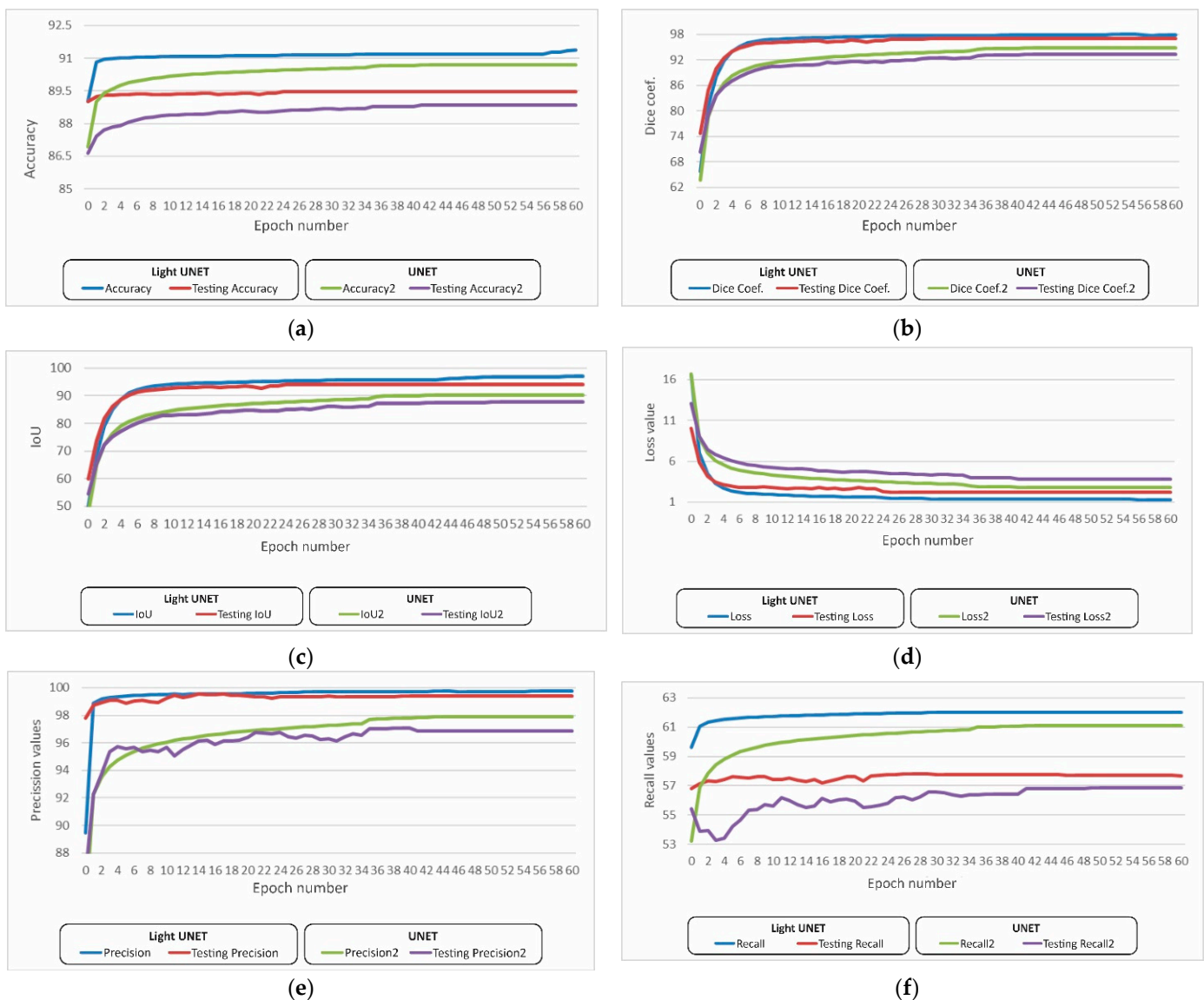


Figure 6. Endocardium segmentation graphical results comparison between novel Light U-Net and the U-net model using training and testing evaluation measures: (a) accuracy, (b) dice metric, (c) IoU, (d) loss value, (e) precision, and (f) recall.

Figure 6c provides the IoU results of the endocardium, which increases swiftly at the start and provides the best results at 60 epochs. The loss values are lower over the training data at the end of each epoch. In Figure 6d, our Light U-Net model provides the minimum

loss at 60 epochs, and initially, until 30 epochs, the value of loss decreases gradually. The proposed algorithm results of precision, as shown in Figure 6e, show a straight jump from lower values to very high values in just a single epoch, after which the change is less as the line in the graph is nearly straight. The recall values of the endocardium are given in Figure 6f, and these curves show a strange order as the recall curve of the U-Net model first decreases and then suddenly increases, while the Light U-Net model provides a complete increase until 60 epochs.

4.2. Experiment 02: LV Epicardium Segmentation Results

The epicardium results are also the most important, as are the endocardium results. Initially, 20 epochs provided an accuracy of 92.6% and a precision ranging to 98.6%. With the upsurge in the number of epochs, it can be seen below in Table 4 that the epicardium results are gaining precision and showing a positive change. Reaching 60 epochs shows complete, accurate and precise values, i.e., with an accuracy of 93.7%, the precision reaches 99.9% and the dice coefficient, 97.1%. Thus, the positive change in the results was the result of increasing the number of epochs.

Table 4. Results of epicardium segmentation using the dataset through the proposed model based on epochs.

Epochs	Accuracy%	Dice Coefficient%	IoU%	Loss%	Precision%
20	0.9262	0.9453	0.9533	0.0241	0.9967
25	0.9264	0.9513	0.9552	0.0229	0.9970
30	0.9265	0.9592	0.9569	0.0218	0.9973
35	0.9264	0.9610	0.9567	0.0221	0.9970
38	0.9268	0.9625	0.9595	0.0202	0.9978
40	0.9269	0.9647	0.9598	0.0200	0.9978
42	0.9270	0.9654	0.9611	0.0192	0.9982
51	0.9273	0.9701	0.9621	0.0186	0.9986
60	0.9370	0.9721	0.9721	0.0150	0.9992

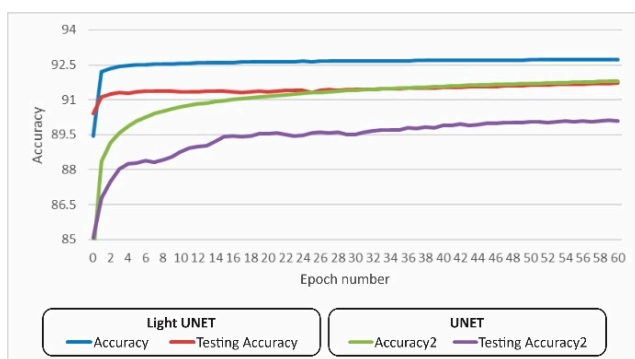
The results of the innovative deep learning method novel Light U-Net applied to the ground truth images are obtained after the mask has been applied. The novel deep-learning technique is producing promising outcomes for all heart slices and for both the systolic and diastolic stages of the heartbeat. To demonstrate the visual results of the novel proposed deep learning model, a few randomly selected images from various cases are provided in Figure 7. The results clearly demonstrate the novel deep learning algorithm's outstanding performance.

Three columns make up Figure 7, as mentioned in the visual results of the endocardium. The ground truth input image of LV is displayed in the first column. The mask is applied to the images of ground truth shown in the second column of the figure. Additionally, the LVOT images, which are difficult to segment, are also responding well to our novel approach. This comparison shows the difference between the implementation of the Light U-Net model against the stock U-Net model for epicardial contours.

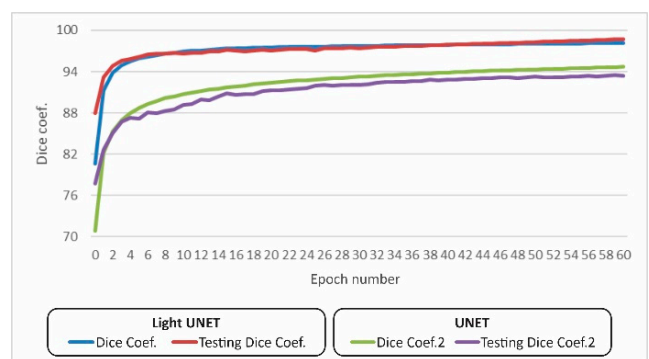
Figure 8 provides the graphical trends of the epicardium against a number of epochs using statistical performance measures as previously mentioned; in the endocardium, the blue and red lines show the results of the novel Light U-Net model. On the other hand, the results from the U-Net model are indicated using green and purple lines. The overall trends in the graph show that the proposed model is yielding better results.

SLICE	INPUT IMAGE WITH GROUND TRUTH	APPLYING GROUND TRUTH MASK	DEEP LEARNING ALGORITHM RESULTS	INPUT IMAGE WITH GROUND TRUTH	APPLYING GROUND TRUTH MASK	DEEP LEARNING ALGORITHM RESULTS
Basel Images						
LVOT Images						
Apical Images						

Figure 7. Segmentation results of endocardium using novel Light U-Net segmentation model.



(a)



(b)

Figure 8. Cont.

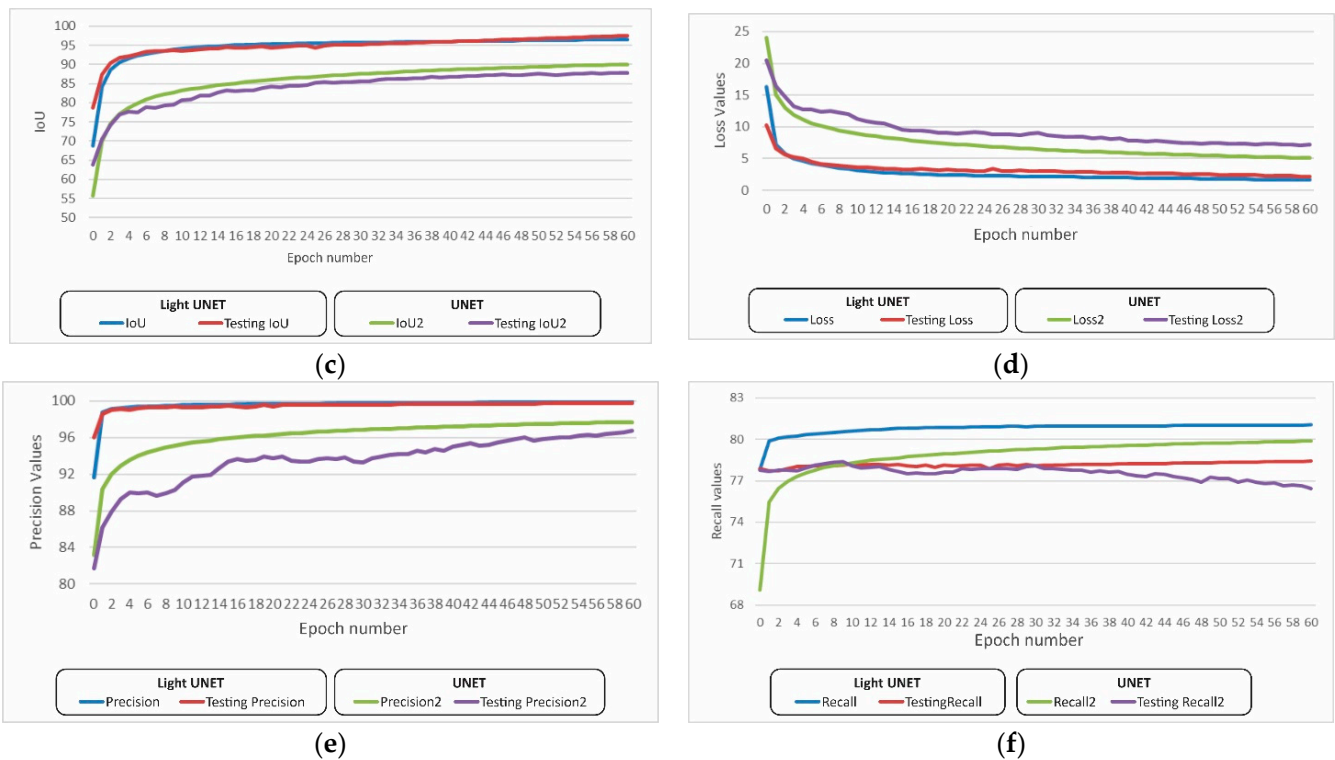


Figure 8. Epicardium segmentation graphical results comparison between novel Light U-Net and the U-Net model using training and testing evaluation measures: (a) accuracy, (b) dice metric, (c) IoU, (d) loss value, (e) precision, and (f) recall.

4.3. Experiment 03: Comparison of Contours Results between Proposed Model and U-Net Model

A comprehensive demonstration of the workflow of the model and its end results is necessary. Simple U-Net architecture is implemented on dataset mask images with ground truth marked on images obtained through the data provided by the Sunnybrook code of evaluation through MATLAB implementation. The resultant segmentation measures produced from both the U-Net implementation and the proposed Light U-Net model are shown in Table 5. For training, the values of the hyperparameters, dataset and evaluation metrics images are used similarly for both models so performances can be compared. Overall, the novel Light U-Net performs well on the LV segmentation challenge. It further shows that the segmented analytical results from the proposed model are on the mark more than those of a simple U-Net, as depicted in Table 5. It shows that using a novel Light U-Net to confine the actual MRI is an essential step that lowers the formulation difficulty, which consequently lowers the likelihood of segmentation errors.

Table 5. Novel Light U-Net and U-Net results comparison for endo- and epicardium contours.

Contours	Model	Epochs	Accuracy	Dice Coeff.	IoU	Precision	Loss
Endocardium	U-Net	66	0.9069	0.9482	0.9022	0.9788	0.0278
	Novel Light U-Net	42	0.9117	0.9779	0.9571	0.9973	0.0137
Epicardium	U-Net	66	0.9196	0.9519	0.9096	0.9808	0.0455
	Novel Light U-Net	30	0.9265	0.9772	0.9569	0.9973	0.0218

4.4. Left Ventricle Segmentation Results of MICCAI Dataset

The results for LV using a deep learning methodology are also evaluated using the publicly available dataset, MICCAI 2009, which has short-axis MRI images that encapsulate all images from the outflow tract to the apical of the heart with the ED to the ES phases of the heart. Each patient’s data is in a separate folder, including the images of a full heart

scan with phases of the heartbeat. This dataset is used for training the model and then its testing. In Table 6 below, selecting 60 epochs provided the accuracy ranging to 0.932 along with precision at 0.9985, Dice matrix at 0.988, IoU at 0.9695 and loss at 0.0135. These results show that if the number of epochs is increased, then the results will be improved.

Table 6. Results of the proposed model for left ventricle segmentation.

Data Set	Accuracy%	Dice Coeff.%	IoU%	Loss%	Precision%	Recall%
Endocardium	0.9270	0.9712	0.9673	0.0120	0.9817	72.01
Epicardium	0.9370	0.9721	0.9721	0.0150	0.9992	82.09
Overall	93.2	97.1	96.95	0.013	99.045	77.05

4.5. Proposed Segmentation Results Comparison with Existing Techniques

To match the performance of the proposed technique, the standard, publicly available dataset, MICCAI 2009, is used. For comparison, relevant state-of-the-art latest methods are considered, such as ResU-Net, half-U-Net, multi-scale, multi-skip, dilated dense, and a combination of CNN and U-Net. Table 7 below illustrates that the proposed method obtained improved performance compared to existing methods.

Table 7. Performance comparison of existing methods with the proposed method.

Ref#	Years	Technique	Dataset	Results (Overall)
[70]	2022	Enhanced ResUnet	MICCAI 2009	DM, APD 0.94 ± 0.04 , 1.48 ± 0.33 mm
[71]	2022	Half-U-Net (U-Net Enabled Encoder Decoder)	MICCAI 2009	Dice coefficient 0.93385
[63]	2021	U-Net combined with image sequence information	MICCAI 2009	DM 93.785
[72]	2020	Dilated dense convolutional network	MICCAI 2009	Dice coefficient 0.94 ± 0.02
[52]	2020	Combined CNN and U-Net	MICCAI 2009	Dice coefficient 0.951
[73]	2019	Convolution based on Sparsity depth-wise U-Net and residual learning	MICCAI 2009	Dice coefficient 0.90
Proposed		Intelligent image enhancement and novel Light U-Net-based segmentation model	MICCAI 2009	Dice coefficient 97.7%

5. Discussion

U-Net is suitable for segmentation problems. Pixel-level information can be preserved by this U-Net and CNN architectures, which is the main reason for choosing these architectures for segmentation. The dataset of MICCAI 2009 images uses four different types of patients with a whole scan of the heart from the apex to the base, and all systolic and diastolic phase data are present in this dataset, along with its ground truths. Obtaining results from the basic U-Net model does not provide better accuracy, so some modifications can enhance the results. The proposed convolutional model was used as a base by adding new layers in a unique minimizing hierarchy, which improved the results. Moreover, enhancement of the data also adds to the good results. The comparison between the U-Net and proposed Light U-Net segmentation models is depicted in the figure below. The input image, along with its ground truth, is used by both models as shown in Figure 9a. Then, a mask is applied in the second step as shown in Figure 9b. The difference in the results of both models is depicted in the figure.

In Figure 9c, the U-Net model segmentation provides rough results, and the obtained images have a distortion in them, while the proposed Light U-Net model as shown in Figure 9d, shows a complete difference and provides enhanced results. Image number 3 in the figure shows LVOT. The LVOT in the U-Net model has not been completely segmented, and the results are not clear. In our model of Light U-Net, the LVOT image is segmented very well and improved as compared to the U-Net model.

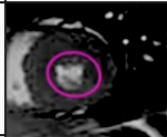



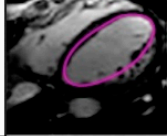



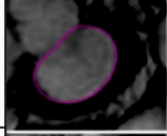



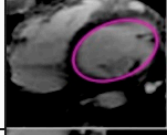
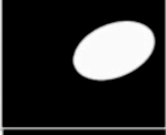

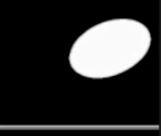
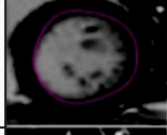



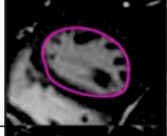



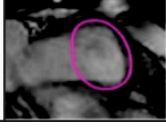



Sr. no	(a) Input with ground truth	(b) Mask	(c) Unet model segmentation result	(d) Proposed model segmentation result
1				
2				
3				
4				
5				
6				
7				

Figure 9. Segmentation results in a comparison between proposed and U-Net models, (a) input with ground truth, (b) mask, (c) U-Net model segmentation results, and (d) proposed model segmentation results.

6. Conclusions and Future Work

This innovative method contributes to processing and normalizing images by performing an intelligent histogram selection of images based on the novel enhancement technique. The novel Light U-net model, having a parallel unique structure of convolutional layers at the encoder side, contributes to the unique architecture of the model. Over the authentic and well-known dataset, the method demonstrated excellent performance and outperformed recent approaches by showing a dice coefficient value of 97.1%. The testing accuracy of the dataset is 92%, and precision is up to 98.17%. The proposed method is intended to eliminate manual and semiautomatic LV segmentation. Deep learning models touching the borders of high levels of accuracy and precision pushed us to deploy neural net learning methods. As per our expectations, the novel approach of U-Net along with the novel enhancement technique, outperformed the recently developed algorithms.

The shape and size of the endocardium and epicardium at the slices of the apical regions and at LVOT are not clearly predictable, which presents significant challenges to the segmentation problem and our model also faces challenges at these stages that must be handled in new techniques by adding or setting parameters for training the network; the use of a vision transformer can also enhance the model. Increases in the testing and training datasets may also contribute to better training configurations.

Author Contributions: Conceptualization, M.I. and M.Y.; Methodology, M.I.S. (Muhammad Imran Sharif) and M.R.; Software, M.I.S. (Muhammad Irfan Sharif); Validation, S.K. All authors have read and agreed to the published version of the manuscript.

Funding: This research received no external funding.

Data Availability Statement: Publicly available dataset is used for evaluation that can be accessed from the link: <https://sourceforge.net/projects/cardiac-mr/files/>.

Conflicts of Interest: The authors declare no conflict of interest.

References

1. Chaudhry, A. Cardiac Deaths May Rise to 23.6 m by 2030: WHO; DAWN, NEWS Report. 753126. *DAWN*, 30 September 2012. Available online: <https://www.dawn.com/news/753126/cardiac-deaths-may-rise-to-23-6m-by-2030-who> (accessed on 18 November 2022).
2. Roth, G.A.; Abate, D.; Abate, K.H.; Abay, S.M.; Abbafati, C.; Abbasi, N.; Abbastabar, H.; Abd-Allah, F.; Abdela, J.; Abdelalim, A. Global, regional, and national age-sex-specific mortality for 282 causes of death in 195 countries and territories, 1980–2017: A systematic analysis for the Global Burden of Disease Study 2017. *Lancet* **2018**, *392*, 1736–1788. [[CrossRef](#)] [[PubMed](#)]
3. Roth, G.A.; Mensah, G.A.; Fuster, V. *The Global Burden of Cardiovascular Diseases and Risks: A Compass for Global Action*; American College of Cardiology Foundation: Washington, DC, USA, 2020; Volume 76, pp. 2980–2981.
4. Irshad, M.; Sharif, M.; Yasmin, M.; Rehman, A.; Khan, M.A. Discrete light sheet microscopic segmentation of left ventricle using morphological tuning and active contours. *Microsc. Res. Tech.* **2022**, *85*, 308–323. [[CrossRef](#)] [[PubMed](#)]
5. Krasnobaev, A.; Sozykin, A. An overview of techniques for cardiac left ventricle segmentation on short-axis MRI. *ITM Web Conf.* **2016**, *8*, 01003. [[CrossRef](#)]
6. Dong, J.; Liu, C.; Yang, C.; Lin, N.; Cao, Y. Robust segmentation of the left ventricle from cardiac MRI via capsule neural network. In Proceedings of the 2nd International Symposium on Image Computing and Digital Medicine, Chengdu, China, 13–14 October 2018; pp. 88–91.
7. Ribeiro, M.A.; Nunes, F.L. Left Ventricle Segmentation in Cardiac MR: A Systematic Mapping of the Past Decade. *ACM Comput. Surv.* **2022**, *54*, 1–38. [[CrossRef](#)]
8. Ruiz-Cano, M.J.; Schramm, R.; Paluszkiwicz, L.; Ramazyan, L.; Rojas, S.V.; Lauenroth, V.; Krenz, A.; Gummert, J.; Morshuis, M. Clinical findings associated with incomplete hemodynamic left ventricular unloading in patients with a left ventricular assist device. *Rev. Esp. Cardiol.* **2022**, *75*, 626–635. [[CrossRef](#)]
9. Pagidipati, N.J.; Gaziano, T.A. Estimating deaths from cardiovascular disease: A review of global methodologies of mortality measurement. *Circulation* **2013**, *127*, 749–756. [[CrossRef](#)]
10. Zotti, C.; Luo, Z.; Lalande, A.; Humbert, O.; Jodoin, P.-M. Novel deep convolution neural network applied to MRI cardiac segmentation. *arXiv* **2017**, arXiv:1705.08943.
11. Kheradmandi, N.; Mehranfar, V. A critical review and comparative study on image segmentation-based techniques for pavement crack detection. *Constr. Build. Mater.* **2022**, *321*, 126162. [[CrossRef](#)]
12. Tang, P.; Yang, P.; Nie, D.; Wu, X.; Zhou, J.; Wang, Y. Unified medical image segmentation by learning from uncertainty in an end-to-end manner. *Knowl. Based Syst.* **2022**, *241*, 108215. [[CrossRef](#)]
13. Zhang, Y.-J. An overview of image and video segmentation in the last 40 years. In *Advances in Image and Video Segmentation*; IGI Global: Hershey, PA, USA, 2006; pp. 1–16.
14. Kang, W.-X.; Yang, Q.-Q.; Liang, R.-P. The comparative research on image segmentation algorithms. In Proceedings of the 2009 First International Workshop on Education Technology and Computer Science, Wuhan, China, 7–8 March 2009; pp. 703–707.
15. Cootes, T.F.; Taylor, C.J.; Cooper, D.H.; Graham, J. Active shape models-their training and application. *Comput. Vis. Image Underst.* **1995**, *61*, 38–59. [[CrossRef](#)]
16. Soliman, A.; Khalifa, F.; Elnakib, A.; Abou El-Ghar, M.; Dunlap, N.; Wang, B.; Gimel'Farb, G.; Keynton, R.; El-Baz, A. Accurate lungs segmentation on CT chest images by adaptive appearance-guided shape modeling. *IEEE Trans. Med. Imaging* **2016**, *36*, 263–276. [[CrossRef](#)]
17. Cootes, T.F.; Edwards, G.J.; Taylor, C.J. Active appearance models. *IEEE Trans. Pattern Anal. Mach. Intell.* **2001**, *23*, 681–685. [[CrossRef](#)]
18. Matthews, I.; Baker, S. Active appearance models revisited. *Int. J. Comput. Vis.* **2004**, *60*, 135–164. [[CrossRef](#)]
19. Cabezas, M.; Oliver, A.; Lladó, X.; Freixenet, J.; Cuadra, M.B. A review of atlas-based segmentation for magnetic resonance brain images. *Comput. Methods Programs Biomed.* **2011**, *104*, e158–e177. [[CrossRef](#)] [[PubMed](#)]
20. Rohlfing, T.; Brandt, R.; Menzel, R.; Russakoff, D.B.; Maurer, C.R. Quo vadis, atlas-based segmentation? In *Handbook of Biomedical Image Analysis*; Springer: New York, NY, USA, 2005; pp. 435–486.
21. Bi, K.; Tan, Y.; Cheng, K.; Chen, Q.; Wang, Y. Sequential shape similarity for active contour based left ventricle segmentation in cardiac cine MR image. *Math. Biosci. Eng.* **2022**, *19*, 1591–1608. [[CrossRef](#)] [[PubMed](#)]
22. Ciyamala Kushbu, S.; Inbamalar, T. Interactive one way contour initialization for cardiac left ventricle and right ventricle segmentation using hybrid method. *J. Med. Imaging Health Inform.* **2021**, *11*, 1037–1054.

23. Faragallah, O.S.; Abdel-Aziz, G.; El-sayed, H.S.; Geweid, G.G. Segmentation of the Left Ventricle in Cardiac MRI Using Random Walk Techniques. *Intell. Autom. Soft Comput.* **2021**, *30*, 575–588. [[CrossRef](#)]
24. Chen, X.; Williams, B.M.; Vallabhaneni, S.R.; Czanner, G.; Williams, R.; Zheng, Y. Learning active contour models for medical image segmentation. In Proceedings of the 2019 IEEE/CVF Conference on Computer Vision and Pattern Recognition, Long Beach, CA, USA, 15–20 June 2019; pp. 11632–11640.
25. Norouzi, A.; Emami, A.; Soroushmehr, S.; Karimi, N.; Samavi, S.; Najarian, K. Left ventricle segmentation By modelling uncertainty in prediction of deep convolutional neural networks and adaptive thresholding inference. *arXiv* **2018**, arXiv:1803.00406.
26. Yang, C.; Wu, W.; Su, Y.; Zhang, S. Left ventricle segmentation via two-layer level sets with circular shape constraint. *Magn. Reson. Imaging* **2017**, *38*, 202–213. [[CrossRef](#)]
27. Shahzad, R.; Gao, S.; Tao, Q.; Dzyubachyk, O.; van der Geest, R. Automated cardiovascular segmentation in patients with congenital heart disease from 3D CMR scans: Combining multi-atlases and level-sets. In *Reconstruction, Segmentation, and Analysis of Medical Images*; Springer: Cham, Switzerland, 2016; pp. 147–155.
28. Johnson, K.W.; Torres Soto, J.; Glicksberg, B.S.; Shameer, K.; Miotto, R.; Ali, M.; Ashley, E.; Dudley, J.T. Artificial intelligence in cardiology. *J. Am. Coll. Cardiol.* **2018**, *71*, 2668–2679. [[CrossRef](#)]
29. Šećkanović, A.; Šehovac, M.; Spahić, L.; Ramić, I.; Mamatnazarova, N.; Pokvić, L.G.; Badnjević, A.; Kacila, M. Review of artificial intelligence application in cardiology. In Proceedings of the 2020 9th Mediterranean Conference on Embedded Computing (MECO), Budva, Montenegro, 8–11 June 2020; pp. 1–5.
30. Winther, H.B.; Hundt, C.; Schmidt, B.; Czerner, C.; Bauersachs, J.; Wacker, F.; Vogel-Claussen, J. v-net: Deep learning for generalized biventricular mass and function parameters using multicenter cardiac MRI data. *JACC Cardiovasc. Imaging* **2018**, *11*, 1036–1038. [[CrossRef](#)] [[PubMed](#)]
31. Dey, D.; Slomka, P.J.; Leeson, P.; Comanicu, D.; Shrestha, S.; Sengupta, P.P.; Marwick, T.H. Artificial intelligence in cardiovascular imaging: JACC state-of-the-art review. *J. Am. Coll. Cardiol.* **2019**, *73*, 1317–1335. [[CrossRef](#)] [[PubMed](#)]
32. Wen, S.; Wei, H.; Yan, Z.; Guo, Z.; Yang, Y.; Huang, T.; Chen, Y. Memristor-based design of sparse compact convolutional neural network. *IEEE Trans. Netw. Sci. Eng.* **2019**, *7*, 1431–1440. [[CrossRef](#)]
33. LeCun, Y.; Bottou, L.; Bengio, Y.; Haffner, P. Gradient-based learning applied to document recognition. *Proc. IEEE* **1998**, *86*, 2278–2324. [[CrossRef](#)]
34. Simonyan, K.; Zisserman, A. Very deep convolutional networks for large-scale image recognition. *arXiv* **2014**, arXiv:1409.1556.
35. Wen, S.; Liu, W.; Yang, Y.; Huang, T.; Zeng, Z. Generating realistic videos from keyframes with concatenated GANs. *IEEE Trans. Circuits Syst. Video Technol.* **2018**, *29*, 2337–2348. [[CrossRef](#)]
36. Zhang, H.; Xu, T.; Li, H.; Zhang, S.; Wang, X.; Huang, X.; Metaxas, D.N. Stackgan++: Realistic image synthesis with stacked generative adversarial networks. *IEEE Trans. Pattern Anal. Mach. Intell.* **2018**, *41*, 1947–1962. [[CrossRef](#)]
37. Oktay, O.; Ferrante, E.; Kamnitsas, K.; Heinrich, M.; Bai, W.; Caballero, J.; Cook, S.A.; De Marvao, A.; Dawes, T.; O’Regan, D.P. Anatomically constrained neural networks (ACNNs): Application to cardiac image enhancement and segmentation. *IEEE Trans. Med. Imaging* **2017**, *37*, 384–395. [[CrossRef](#)]
38. Liu, M.; Zhou, Z.; Shang, P.; Xu, D. Fuzzified image enhancement for deep learning in iris recognition. *IEEE Trans. Fuzzy Syst.* **2019**, *28*, 92–99. [[CrossRef](#)]
39. Goodfellow, I.; Bengio, Y.; Courville, A. *Deep Learning*; MIT Press: Cambridge, MA, USA, 2016.
40. Bernard, O.; Lalande, A.; Zotti, C.; Cervenansky, F.; Yang, X.; Heng, P.-A.; Cetin, I.; Lekadir, K.; Camara, O.; Ballester, M.A.G. Deep learning techniques for automatic MRI cardiac multi-structures segmentation and diagnosis: Is the problem solved? *IEEE Trans. Med. Imaging* **2018**, *37*, 2514–2525. [[CrossRef](#)]
41. Dong, Z.; Du, X.; Liu, Y. Automatic segmentation of left ventricle using parallel end–end deep convolutional neural networks framework. *Knowl. Based Syst.* **2020**, *204*, 106210. [[CrossRef](#)]
42. Dangi, S.; Linte, C.A.; Yaniv, Z. A distance map regularized CNN for cardiac cine MR image segmentation. *Med. Phys.* **2019**, *46*, 5637–5651. [[CrossRef](#)]
43. Zhang, D.; Icke, I.; Dogdas, B.; Parimal, S.; Sampath, S.; Forbes, J.; Bagchi, A.; Chin, C.-L.; Chen, A. A multi-level convolutional LSTM model for the segmentation of left ventricle myocardium in infarcted porcine cine MR images. In Proceedings of the 2018 IEEE 15th International Symposium on Biomedical Imaging (ISBI 2018), Washington, DC, USA, 4–7 April 2018; pp. 470–473.
44. Merjulah, R.; Chandra, J. Segmentation technique for medical image processing: A survey. In Proceedings of the 2017 International Conference on Inventive Computing and Informatics (ICICI), Coimbatore, India, 23–24 November 2017; pp. 1055–1061.
45. Tran, P.V. A fully convolutional neural network for cardiac segmentation in short-axis MRI. *arXiv* **2016**, arXiv:1604.00494.
46. Rostami, A.; Amirani, M.C.; Yousef-Banaem, H. Segmentation of the left ventricle in cardiac MRI based on convolutional neural network and level set function. *Health Technol.* **2020**, *10*, 1155–1162. [[CrossRef](#)]
47. Nguyen, N.M.; Ray, N. End-to-end learning of convolutional neural net and dynamic programming for left ventricle segmentation. In Proceedings of the Third Conference on Medical Imaging with Deep Learning, Montreal, QC, Canada, 6–8 July 2020; pp. 555–569.
48. Kayalibay, B.; Jensen, G.; van der Smagt, P. CNN-based segmentation of medical imaging data. *arXiv* **2017**, arXiv:1701.03056.
49. Chang, Y.; Jung, C. Automatic cardiac MRI segmentation and permutation-invariant pathology classification using deep neural networks and point clouds. *Neurocomputing* **2020**, *418*, 270–279. [[CrossRef](#)]

50. Tan, L.K.; Liew, Y.M.; Lim, E.; McLaughlin, R.A. Convolutional neural network regression for short-axis left ventricle segmentation in cardiac cine MR sequences. *Med. Image Anal.* **2017**, *39*, 78–86. [[CrossRef](#)]
51. Lin, A.; Wu, J.; Yang, X. A data augmentation approach to train fully convolutional networks for left ventricle segmentation. *Magn. Reson. Imaging* **2020**, *66*, 152–164. [[CrossRef](#)]
52. Wu, B.; Fang, Y.; Lai, X. Left ventricle automatic segmentation in cardiac MRI using a combined CNN and U-net approach. *Comput. Med. Imaging Graph.* **2020**, *82*, 101719. [[CrossRef](#)]
53. Xie, L.; Song, Y.; Chen, Q. Automatic left ventricle segmentation in short-axis MRI using deep convolutional neural networks and central-line guided level set approach. *Comput. Biol. Med.* **2020**, *122*, 103877. [[CrossRef](#)]
54. Krizhevsky, A.; Sutskever, I.; Hinton, G.E. Imagenet classification with deep convolutional neural networks. In Proceedings of the Advances in Neural Information Processing Systems 25: 26th Annual Conference on Neural Information Processing Systems 2012, Lake Tahoe, NV, USA, 3–6 December 2012.
55. Wang, Z.; Xie, L.; Qi, J. Dynamic pixel-wise weighting-based fully convolutional neural networks for left ventricle segmentation in short-axis MRI. *Magn. Reson. Imaging* **2020**, *66*, 131–140. [[CrossRef](#)] [[PubMed](#)]
56. Luo, Y.; Yang, B.; Xu, L.; Hao, L.; Liu, J.; Yao, Y.; van de Vosse, F. Segmentation of the left ventricle in cardiac MRI using a hierarchical extreme learning machine model. *Int. J. Mach. Learn. Cybern.* **2018**, *9*, 1741–1751. [[CrossRef](#)]
57. Li, Z.; Lin, A.; Yang, X.; Wu, J. Left ventricle segmentation by combining convolution neural network with active contour model and tensor voting in short-axis MRI. In Proceedings of the 2017 IEEE International Conference on Bioinformatics and Biomedicine (BIBM), Kansas City, MO, USA, 13–16 November 2017; pp. 736–739.
58. Yang, X.; Gobeawan, L.; Yeo, S.Y.; Tang, W.T.; Wu, Z.; Su, Y. Automatic segmentation of left ventricular myocardium by deep convolutional and de-convolutional neural networks. In Proceedings of the 2016 Computing in Cardiology Conference (CinC), Vancouver, BC, Canada, 11–14 September 2016; pp. 81–84.
59. Dong, S.; Luo, G.; Wang, K.; Cao, S.; Li, Q.; Zhang, H. A combined fully convolutional networks and deformable model for automatic left ventricle segmentation based on 3D echocardiography. *BioMed Res. Int.* **2018**, *2018*, 5682365. [[CrossRef](#)] [[PubMed](#)]
60. Mehta, R.; Sivaswamy, J. M-net: A convolutional neural network for deep brain structure segmentation. In Proceedings of the 2017 IEEE 14th International Symposium on Biomedical Imaging (ISBI 2017), Melbourne, VIC, Australia, 18–21 April 2017; pp. 437–440.
61. Das, N.; Das, S. Cardiac MRI Segmentation Using Deep Learning. *Res. Sq.* **2022**, *Epub ahead of printing*. [[CrossRef](#)]
62. Yang, R.; Yu, J.; Yin, J.; Liu, K.; Xu, S. A dense R-CNN multi-target instance segmentation model and its application in medical image processing. *IET Image Process.* **2022**, *16*, 2495–2505. [[CrossRef](#)]
63. Wang, Y.; Zhang, Y.; Wen, Z.; Tian, B.; Kao, E.; Liu, X.; Xuan, W.; Ordovas, K.; Saloner, D.; Liu, J. Deep learning based fully automatic segmentation of the left ventricular endocardium and epicardium from cardiac cine MRI. *Quant. Imaging Med. Surg.* **2021**, *11*, 1600. [[CrossRef](#)]
64. Abdeltawab, H.; Khalifa, F.; Taher, F.; Beache, G.; Mohamed, T.; Elmaghraby, A.; Ghazal, M.; Keynton, R.; El-Baz, A. A novel deep learning approach for left ventricle automatic segmentation in cardiac cine mr. In Proceedings of the 2019 Fifth International Conference on Advances in Biomedical Engineering (ICABME), Tripoli, Lebanon, 17–19 October 2019; pp. 1–4.
65. Chang, Y.; Song, B.; Jung, C.; Huang, L. Automatic segmentation and cardiopathy classification in cardiac MRI images based on deep neural networks. In Proceedings of the 2018 IEEE International Conference on Acoustics, Speech and Signal Processing (ICASSP), Calgary, AB, Canada, 15–20 April 2018; pp. 1020–1024.
66. Gao, S.; Bui, T.D. Image segmentation and selective smoothing by using Mumford-Shah model. *IEEE Trans. Image Process.* **2005**, *14*, 1537–1549.
67. Deng, J.; Dong, W.; Socher, R.; Li, L.-J.; Li, K.; Fei-Fei, L. Imagenet: A large-scale hierarchical image database. In Proceedings of the 2009 IEEE Conference on Computer Vision and Pattern Recognition, Miami, FL, USA, 20–25 June 2009; pp. 248–255.
68. Abadi, M.; Barham, P.; Chen, J.; Chen, Z.; Davis, A.; Dean, J.; Devin, M.; Ghemawat, S.; Irving, G.; Isard, M. TensorFlow: A system for Large-Scale machine learning. In Proceedings of the 12th USENIX Symposium On Operating Systems Design and Implementation (OSDI 16), Savannah, GA, USA, 2–4 November 2016; pp. 265–283.
69. Choi, K.; Joo, D.; Kim, J. Kapre: On-gpu audio preprocessing layers for a quick implementation of deep neural network models with keras. *arXiv* **2017**, arXiv:1706.05781.
70. Xu, S.; Lu, H.; Cheng, S.; Pei, C. Left Ventricle Segmentation in Cardiac MR Images via an Improved ResUnet. *Int. J. Biomed. Imaging* **2022**, *2022*, 8669305. [[CrossRef](#)]
71. Lu, H.; She, Y.; Tie, J.; Xu, S. Half-UNet: A Simplified U-Net Architecture for Medical Image Segmentation. *Front. Neuroinform.* **2022**, *16*, 911679. [[CrossRef](#)]
72. Xu, S.; Cheng, S.; Min, X.; Pan, N.; Hu, H. Left Ventricle Segmentation Based on a Dilated Dense Convolutional Networks. *IEEE Access* **2020**, *8*, 214087–214097. [[CrossRef](#)]
73. Curiale, A.H.; Colavecchia, F.D.; Mato, G. Automatic quantification of the LV function and mass: A deep learning approach for cardiovascular MRI. *Comput. Methods Programs Biomed.* **2019**, *169*, 37–50. [[CrossRef](#)] [[PubMed](#)]

Disclaimer/Publisher’s Note: The statements, opinions and data contained in all publications are solely those of the individual author(s) and contributor(s) and not of MDPI and/or the editor(s). MDPI and/or the editor(s) disclaim responsibility for any injury to people or property resulting from any ideas, methods, instructions or products referred to in the content.